

NUMERICAL SIMULATION OF PULSE-LIKE NEAR-FAULT GROUND MOTIONS

Juin-Fu Chai and Tsung-Jen Teng

National Center for Research on Earthquake Engineering, Taipei, Taiwan

chai@ncree.gov.tw, tjteng@ncree.gov.tw

Abstract

The simulation of representative pulse-like near-fault ground motions for the purpose of assessing near-fault effect is developed in the current study. Firstly, in this paper, a 3D quasi-dynamic model is developed to simulate the rupture and healing processes of a fault plane. Due to the different healing times defined by the proposed space-time slip function for all rupture points on the fault plane, the induced rupture snapshots are strongly asymmetric, and the rupture growth is intermediate between a circular rupture and a unilaterally propagating rupture. After that, based on the integral representation theory, the ground motions of a three dimensional half-space can be determined by means of the slip function of a buried fault plane as well as the Green's function due to a unit point source within the half-space. In consequence of the directivity effect, the typical pulse-like velocity waveforms can be found within the near-fault area where the rupture front and healing front are close to each other to cause interference. In addition, corresponding to the representative pulse-like ground motions, the near-fault structural response spectra are carried out to show the attenuation of required spectral demands for designing structures against the near-fault ground motions.

INTRODUCTION

Near-fault ground motions, which have caused severe damages in recent disastrous earthquakes, are characterized by a short-duration impulsive motion that will transmit large energy into the structures at the beginning of the earthquake. It has been shown that the response of structures subjected to an observed near-fault ground motion is much similar to that subjected to an equivalent pulse-like motion (Alavi and Krawinkler, 2000). Therefore, for the purpose of assessing near-fault effects, a quasi-dynamic rupture model that reflects all of the physical realities of a buried dip-slip fault is developed in this paper to generate the representative pulse-like near-fault ground motions instead of the observed ones.

In fact, the pulse-like velocity waveform is owing to the directivity effect where the rupture front and healing front are close to each other to cause interference at that site (Somerville *et al*, 1997). Therefore, both the rupture and healing processes should be included in the rupture model of a buried fault plane (Madariaga, 1976; Boatwright, 1981). In this paper, a 3D quasi-dynamic rupture model is proposed. For each point on the fault plane, it begins to slip when the crack tip arrives from the hypocenter with a constant rupture speed, and the slip velocity will approach a constant soon and then

deaccelerate to become zero. Because of the different healing time at each point, the induced rupture snapshots are strongly asymmetric and the rupture growth is intermediate between a circular rupture and a unilaterally propagating rupture.

Based on the integral representation theory (Pao and Varatharajulu, 1976), the ground motions of a three dimensional half-space can be determined by means of the slip function of a buried fault plane as well as the Green's function due to a unit point source within the half-space. It can be found from the synthetic time histories of the near-fault ground motions that the pulse-like velocity waveforms exist within the affected range of directivity effect. In addition, the response spectra caused by the representative pulse-like ground motions are also determined to show the required spectral demand caused by near-fault ground motions.

QUASI-DYNAMIC RUPTURE MODEL

Consider a dip-slip fault plane, the location of each point on the plane can be defined by the position vector $\mathbf{x}=(\mathbf{x},h)$ as shown in Fig. 1. The origin of the local coordinates is coincident with the hypocenter and the slip dislocation is along the x -axis. For each point \mathbf{x} , it begins to slip when the crack tip arrives from the hypocenter with a constant rupture speed v , and the slip velocity will approach a constant V_0 soon to represent the continuation of the self-similar slip distribution. Then, a causal healing behavior begins to stop the rupture growth. The slip velocity $V(\mathbf{x},t)$ can be defined by

$$V(\xi,t) = \begin{cases} 0 & ; 0 \leq t \leq T_r(\xi) \\ \frac{V_0 t}{\sqrt{t^2 - T_r^2}} & ; T_r(\xi) \leq t \leq T_s(\xi) \\ \frac{T_h - t}{D} \frac{V_0 t}{\sqrt{t^2 - T_r^2}} & ; T_s(\xi) \leq t \leq T_h(\xi) \\ 0 & ; T_h(\xi) \leq t \end{cases} \quad \text{with } \begin{cases} T_r(\xi) = |\xi|/v \\ T_h(\xi) = T_0 - |\xi - \xi_0|/b \\ T_s(\xi) = T_h(\xi) - D(\xi) \end{cases} \quad (1)$$

Herein, $T_r(\mathbf{x})$ and $T_s(\mathbf{x})$ are the times of the onset of rupturing and healing at \mathbf{x} , respectively, $T_h(\mathbf{x})$ is the time that the rupture heals, and $D(\mathbf{x})$ is the healing interval. In addition, $T_0=T_h(\mathbf{x}_0)$ is the faulting duration, b is the healing speed that is specified as the shear wave velocity, and $\mathbf{x}_0=(x_0,0)$ is the last point of the rupture to heal.

Specifying the rupture end on the positive x -axis (toward the ground surface) as $\mathbf{x}_R=(x_R,0)$, then the faulting duration T_0 can be determined from $T_r(\mathbf{x}_R)=T_h(\mathbf{x}_R)$ as

$$T_0 = \frac{x_R}{v} + \frac{x_R - x_0}{b} \quad (2)$$

As shown in Fig. 1, the boundary G of the rupture range on the fault plane can be defined by $\xi_r = (x_0 + R \cos q, R \sin q)$, and further, the function $R(q)$ can be determined from $T_r(\mathbf{x}_G)=T_h(\mathbf{x}_G)$ as

$$R(q) = \frac{b}{b^2 - v^2} \left[\sqrt{(x_0 b \cos q + v^2 T_0)^2 - (b^2 - v^2)(x_0^2 - v^2 T_0^2)} - (x_0 b \cos q + v^2 T_0) \right] \quad (3)$$

It can be found that the extent of the rupture is asymmetric about the hypocenter, and the rupture

growth is intermediate between a circular rupture and a unilaterally propagating rupture. However, it is noted that the rupture is symmetric about the x -axis. The healing interval $D(x)$ is defined as D_0 at x_0 , and then decreases linearly to become zero on the boundary G . Therefore, as shown in Fig. 1, the healing interval $D(x)$ for a point $x=(x,h)$ within the rupture range can be defined by

$$D(\xi) = D_0 \cdot \frac{R(q) - r}{R(q)} \quad \text{with} \quad r = |\xi - \xi_0| \quad ; \quad q = \cos^{-1} \left(\frac{x - x_0}{r} \right) \quad (4)$$

Figure 2 shows the space-time diagram of the rupture growth and healing of the adopted source model for the points along x -axis. The fault is slipping inside the region bounded by the lines $T_r(x)$ and $T_h(x)$, and is healing in the gray region of $T_s(x) < t < T_h(x)$. Finally, the slip dislocation function can be defined from Eq. 1 as

$$D(\xi, t) = \begin{cases} 0 & ; 0 \leq t \leq T_r(\xi) \\ V_0 \sqrt{t^2 - T_r^2} & ; T_r(\xi) \leq t \leq T_s(\xi) \\ \frac{V_0}{D} \left[\left(T_h - \frac{t}{2} \right) \sqrt{t^2 - T_r^2} - \frac{T_s}{2} \sqrt{T_s^2 - T_r^2} - \frac{T_r^2}{2} \ln \left(\frac{t + \sqrt{t^2 - T_r^2}}{T_s + \sqrt{T_s^2 - T_r^2}} \right) \right] & ; T_s(\xi) \leq t \leq T_h(\xi) \\ \frac{V_0}{D} \left[\frac{T_h}{2} \sqrt{T_h^2 - T_r^2} - \frac{T_s}{2} \sqrt{T_s^2 - T_r^2} - \frac{T_r^2}{2} \ln \left(\frac{T_h + \sqrt{T_h^2 - T_r^2}}{T_s + \sqrt{T_s^2 - T_r^2}} \right) \right] & ; T_h(\xi) \leq t \end{cases} \quad (5)$$

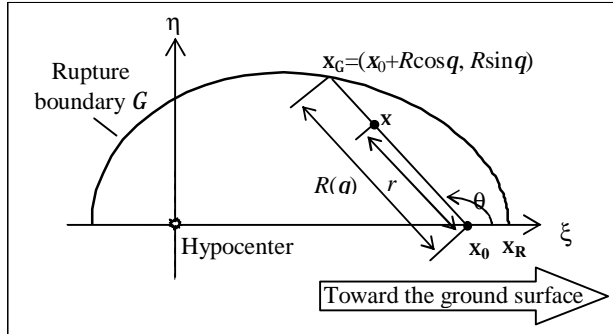


Fig. 1: Local coordinates on the fault plane

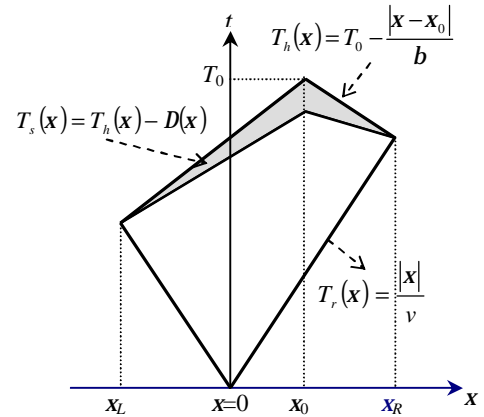


Fig. 2: The space-time diagram of the rupture growth and healing

NEAR-FAULT GROUND MOTIONS

Integral Representation Theory

As shown in Fig. 3, a fault plane Σ is defined in the half-space with a dipping angle d . Consider the global Cartesian coordinates $(x-y-z)$ system, the y -axis is defined as the intersection of the fault plane and the free surface, and the later is defined by $z=0$. In addition, a local Cartesian coordinates $(x-h-z)$ system is defined on the fault plane ($z=0$) with the origin being coincident with the hypocenter. The x -axis is along the slip dislocation, and the angle between x -axis and y' -axis (parallel to y -axis) on the

fault plane is defined by \mathbf{a} . Therefore, the transform relationship between the unit vectors of the global and local coordinates can be expressed by

$$\begin{aligned} \mathbf{e}_\xi &= \sin a \cos d \mathbf{e}_x + \cos a \mathbf{e}_y - \sin a \sin d \mathbf{e}_z \\ \mathbf{e}_\eta &= -\cos a \cos d \mathbf{e}_x + \sin a \mathbf{e}_y + \cos a \sin d \mathbf{e}_z \\ \mathbf{e}_\zeta &= \sin d \mathbf{e}_x + \cos d \mathbf{e}_z \end{aligned} \quad (6)$$

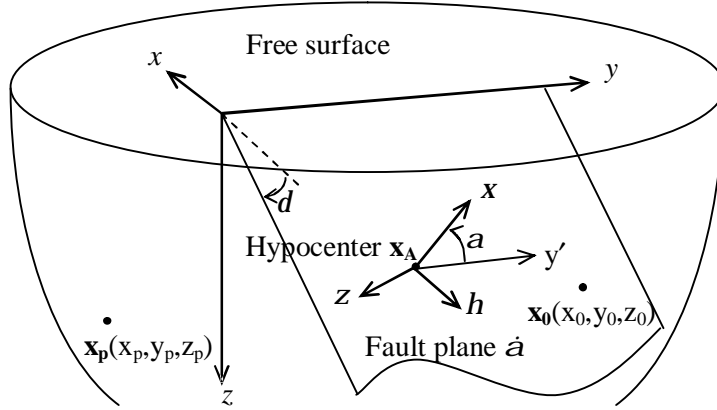


Fig. 3: Global and local coordinates in the 3D half-space for the near-fault analysis

Based on the integral representation theory, the induced displacement components at \mathbf{x}_p outside the fault plane can be expressed by the Voigt form as

$$u_i(\mathbf{x}_p) = \int_S [u_j(\mathbf{x}_0)] S_{jk}^{Gi}(\mathbf{x}_0; \mathbf{x}_p) n_k dS \quad ; \quad \mathbf{x}_p \notin S \quad (7)$$

where $[u_j(\mathbf{x}_0)]$ is the slip dislocation at rupture point \mathbf{x}_0 on the fault plane, $S_{jk}^{Gi}(\mathbf{x}_0; \mathbf{x}_p)$ is the stress at \mathbf{x}_0 induced by a unit point force loaded along \mathbf{e}_i at \mathbf{x}_p , and n_k is the unit normal of the fault plane. Based on the local coordinates, because $[u_h(\mathbf{x}_0)] = [u_z(\mathbf{x}_0)] = 0$ at each rupture point $\mathbf{x}_0 = (x_0, h_0, 0)$ and $n_z = 1$ with $n_x = n_h = 0$, Eq. (7) can be simplified by

$$\begin{aligned} u_x(\xi_p) &= \int_S [u_x(\xi_0)] S_{xz}^{Gx}(\xi_0; \xi_p) dx_0 dh_0 \quad ; \quad \xi_p \notin S \\ u_h(\xi_p) &= \int_S [u_x(\xi_0)] S_{xz}^{Gh}(\xi_0; \xi_p) dx_0 dh_0 \quad ; \quad \xi_p \notin S \\ u_z(\xi_p) &= \int_S [u_x(\xi_0)] S_{xz}^{Gz}(\xi_0; \xi_p) dx_0 dh_0 \quad ; \quad \xi_p \notin S \end{aligned} \quad (8)$$

Based on the rotation transformation of displacement and force components between global and local coordinate systems as well as the train rule, the induced displacement at \mathbf{x}_p outside the fault plane can be expressed as

$$\begin{Bmatrix} u_x(\mathbf{x}_p) \\ u_y(\mathbf{x}_p) \\ u_z(\mathbf{x}_p) \end{Bmatrix} = m \int_S [u_x(x_0, h_0)] \begin{Bmatrix} E_x(\mathbf{x}_0; \mathbf{x}_p) \\ E_y(\mathbf{x}_0; \mathbf{x}_p) \\ E_z(\mathbf{x}_0; \mathbf{x}_p) \end{Bmatrix} dx_0 dh_0 \quad (9)$$

where m is the shear modulus of the half-space. Parameter $E_x(\mathbf{x}_0; \mathbf{x}_p)$ is defined by

$$E_x(\mathbf{x}_0; \mathbf{x}_p) = \sin a \left[\sin 2\delta \left(\frac{\partial u_x^{Gx}(\mathbf{x}; \mathbf{x}_p)}{\partial x} - \frac{\partial u_z^{Gx}(\mathbf{x}; \mathbf{x}_p)}{\partial z} \right) + \cos 2d \left(\frac{\partial u_x^{Gx}(\mathbf{x}; \mathbf{x}_p)}{\partial z} + \frac{\partial u_z^{Gx}(\mathbf{x}; \mathbf{x}_p)}{\partial x} \right) \right]_{\mathbf{x}=\mathbf{x}_0} \quad (10)$$

$$+ \cos a \left[\sin \delta \left(\frac{\partial u_y^{Gx}(\mathbf{x}; \mathbf{x}_p)}{\partial x} + \frac{\partial u_x^{Gx}(\mathbf{x}; \mathbf{x}_p)}{\partial y} \right) + \cos d \left(\frac{\partial u_y^{Gx}(\mathbf{x}; \mathbf{x}_p)}{\partial z} + \frac{\partial u_z^{Gx}(\mathbf{x}; \mathbf{x}_p)}{\partial y} \right) \right]_{\mathbf{x}=\mathbf{x}_0}$$

where $u_x^{Gx}(\mathbf{x}; \mathbf{x}_p)$, $u_y^{Gx}(\mathbf{x}; \mathbf{x}_p)$ and $u_z^{Gx}(\mathbf{x}; \mathbf{x}_p)$ denote the displacement components (global x - y - z coordinates) at \mathbf{x} induced by a unit point force loaded along \mathbf{e}_x at \mathbf{x}_p . The other two parameters E_y and E_z can be defined by Eq. (10) while the superscript ‘ Gx ’ of the displacement components being replaced by ‘ Gy ’ and ‘ Gz ’ to represent the unit point force loaded along \mathbf{e}_y and \mathbf{e}_z , respectively. In addition, the rupture point $\mathbf{x}_0=(x_0, y_0, z_0)$ on the fault plane can be expressed by the local coordinates as

$$\begin{aligned} x_0 &= x_A + \mathbf{x}_0 \sin a \cos d - h_0 \cos a \cos d \\ y_0 &= y_A + \mathbf{x}_0 \cos a + h_0 \sin a \\ z_0 &= z_A - \mathbf{x}_0 \sin a \sin d + h_0 \cos a \sin d \end{aligned} \quad (11)$$

where $\mathbf{x}_A=(x_A, y_A, z_A)$ denotes the hypocenter.

Solution due to Unit Point Force in Half-space

Based on the global x - y - z coordinates, the displacement can be defined by the scalar potentials f , c and y as

$$\mathbf{u} = \nabla f + \nabla \times \nabla \times (0, 0, c) + \nabla \times (0, 0, y) \quad (12)$$

All of the potentials satisfy the Helmholtz equations in frequency domain. For a point source located at \mathbf{x}_p in a half-space, the induced potentials at \mathbf{x} can be expressed in the frequency domain by

$$\begin{aligned} \bar{f}_H(\mathbf{x}; \mathbf{x}_p, w) &= \bar{f}_0(\mathbf{x}; \mathbf{x}_p, w) + \bar{f}_r(\mathbf{x}; \mathbf{x}_p, w) \\ \bar{c}_H(\mathbf{x}; \mathbf{x}_p, w) &= \bar{c}_0(\mathbf{x}; \mathbf{x}_p, w) + \bar{c}_r(\mathbf{x}; \mathbf{x}_p, w) \\ \bar{y}_H(\mathbf{x}; \mathbf{x}_p, w) &= \bar{y}_0(\mathbf{x}; \mathbf{x}_p, w) + \bar{y}_r(\mathbf{x}; \mathbf{x}_p, w) \end{aligned} \quad (13)$$

where \bar{f}_0 , \bar{c}_0 and \bar{y}_0 are the solutions in an infinite space, \bar{f}_r , \bar{c}_r and \bar{y}_r are the terms reflected from the free surface ($z=0$). Considering the Fourier transformations between wavenumber and special coordinate as well as the radiation conditions due to a point source, the general solutions of scalar potentials can be solved and expressed by a double integral representation form as

$$\begin{aligned} \bar{f}_0(\mathbf{x}; \mathbf{x}_p, w) &= \frac{1}{4p^2} \int_{-\infty}^{\infty} \int_{-\infty}^{\infty} A_0 e^{-n|z-z_p| - ik_x(x-x_p) - ik_y(y-y_p)} dk_x dk_y \\ \bar{c}_0(\mathbf{x}; \mathbf{x}_p, w) &= \frac{1}{4p^2} \int_{-\infty}^{\infty} \int_{-\infty}^{\infty} B_0 e^{-n|z-z_p| - ik_x(x-x_p) - ik_y(y-y_p)} dk_x dk_y \\ \bar{y}_0(\mathbf{x}; \mathbf{x}_p, w) &= \frac{1}{4p^2} \int_{-\infty}^{\infty} \int_{-\infty}^{\infty} C_0 e^{-n|z-z_p| - ik_x(x-x_p) - ik_y(y-y_p)} dk_x dk_y \end{aligned} \quad (14a)$$

$$\begin{aligned}
\bar{f}_r(\mathbf{x}; \mathbf{x}_p, w) &= \frac{1}{4p^2} \int_{-\infty}^{\infty} \int_{-\infty}^{\infty} A_r e^{-nz - ik_x(x-x_p) - ik_y(y-y_p)} dk_x dk_y \\
\bar{c}_r(\mathbf{x}; \mathbf{x}_p, w) &= \frac{1}{4p^2} \int_{-\infty}^{\infty} \int_{-\infty}^{\infty} B_r e^{-n'z - ik_x(x-x_p) - ik_y(y-y_p)} dk_x dk_y \\
\bar{y}_r(\mathbf{x}; \mathbf{x}_p, w) &= \frac{1}{4p^2} \int_{-\infty}^{\infty} \int_{-\infty}^{\infty} C_r e^{-n'z - ik_x(x-x_p) - ik_y(y-y_p)} dk_x dk_y
\end{aligned} \tag{14b}$$

where

$$n = \sqrt{k_x^2 + k_y^2 - k_p^2} \quad ; \quad n' = \sqrt{k_x^2 + k_y^2 - k_s^2} \tag{15}$$

In addition, based on the traction free conditions on the free surface ($z=0$), the coefficients A_r , B_r and C_r of the reflected terms can be solved and expressed in terms of A_0 , B_0 and C_0 as

$$A_r = R_{pp} A_0^- e^{-nz_p} + R_{ps} B_0^- e^{-n'z_p} \quad ; \quad B_r = R_{sp} A_0^- e^{-nz_p} + R_{ss} B_0^- e^{-n'z_p} \quad ; \quad C_r = C_0^- e^{-n'z_p} \tag{16}$$

herein, the reflected coefficients R_{pp} , R_{ps} , R_{sp} and R_{ss} are defined by

$$\begin{aligned}
R_{pp} = R_{ss} &= -\frac{1}{F} \left[(2k^2 - k_s^{*2})^2 + 4mn'k^2 \right] \\
R_{ps} &= -\frac{1}{F} \left[4n'k^2 (2k^2 - k_s^{*2}) \right] \quad ; \quad R_{sp} = -\frac{1}{F} \left[4n(2k^2 - k_s^{*2}) \right]
\end{aligned} \tag{17}$$

while F being the Rayleigh function defined by

$$F = (2k^2 - k_s^2)^2 - 4k^2 n n' \quad \text{with} \quad k^2 = k_x^2 + k_y^2 \tag{18}$$

Furthermore, it should be noted that the superscript $'$ of A_0^- , B_0^- and C_0^- in Eq. (16) implies that the coefficients of solutions in infinite domain should be evaluated under the condition of $(z-z_p) < 0$.

Consider the unit point forces along \mathbf{e}_x , \mathbf{e}_y and \mathbf{e}_z , respectively, the associated coefficients of the potentials in an infinite domain can be solved as

$$\begin{aligned}
A_0^x &= \frac{ik_x}{2nk_s^{*2} m} \quad ; \quad B_0^x = \frac{ik_x}{2k^2 k_s^{*2} m} \text{sgn}(z - z_p) \quad ; \quad C_0^x = \frac{ik_y}{2k^2 n' m} \\
A_0^y &= \frac{ik_y}{2nk_s^{*2} m} \quad ; \quad B_0^y = \frac{ik_y}{2k^2 k_s^{*2} m} \text{sgn}(z - z_p) \quad ; \quad C_0^y = -\frac{ik_x}{2k^2 n' m} \\
A_0^z &= \frac{1}{2k_s^{*2} m} \text{sgn}(z - z_p) \quad ; \quad B_0^z = \frac{1}{2k_s^{*2} n' m} \quad ; \quad C_0^z = 0
\end{aligned} \tag{19}$$

Therefore, the displacements $\bar{\mathbf{u}}^{\text{Gx}}(\mathbf{x}; \mathbf{x}_p)$, $\bar{\mathbf{u}}^{\text{Gy}}(\mathbf{x}; \mathbf{x}_p)$ and $\bar{\mathbf{u}}^{\text{Gz}}(\mathbf{x}; \mathbf{x}_p)$ at \mathbf{x} due to the unit point forces loaded at \mathbf{x}_p along \mathbf{e}_x , \mathbf{e}_y and \mathbf{e}_z , respectively, can be determined straightforwardly by Eqs. (12)-(19).

Near-fault Ground Motions

Then, based on the displacements due to the unit point forces loaded along \mathbf{e}_x , \mathbf{e}_y and \mathbf{e}_z , the associated parameters $\bar{E}_x(\mathbf{x}_0; \mathbf{x}_p)$, $\bar{E}_y(\mathbf{x}_0; \mathbf{x}_p)$ and $\bar{E}_z(\mathbf{x}_0; \mathbf{x}_p)$ can be determined by Eq. (10), and subsequently, the induced near-fault displacement $\mathbf{u}(\mathbf{x}_p)$ with \mathbf{x}_p outside the fault plane can be determined by Eq. (9). Let $\mathbf{x}_p=(x,y,0)$ approach the free surface, the ground displacement components caused by the rupture of a fault plane can be determined in the frequency domain and expressed by the double integral representation form as

$$\begin{aligned}
\bar{u}_x(\mathbf{x}_p, w) &= \int_S [\bar{u}_x(\mathbf{x}_0, w)] \left\{ \frac{1}{4p^2} \int_{-\infty}^{\infty} \int_{-\infty}^{\infty} \left[\frac{2ik_x \mathbf{n}'}{F} \right] A^* e^{-n z_0 - ik_x(x-x_0) - ik_y(y-y_0)} dk_x dk_y \right. \\
&\quad + \frac{1}{4p^2} \int_{-\infty}^{\infty} \int_{-\infty}^{\infty} \left[\frac{ik_x(2k^2 - k_s^{*2})}{Fk^2} \right] B^* e^{-n z_0 - ik_x(x-x_0) - ik_y(y-y_0)} dk_x dk_y \\
&\quad \left. + \frac{1}{4p^2} \int_{-\infty}^{\infty} \int_{-\infty}^{\infty} \left[-\frac{ik_y}{k^2 \mathbf{n}'} \right] C^* e^{-n z_0 - ik_x(x-x_0) - ik_y(y-y_0)} dk_x dk_y \right\} d\mathbf{x}_0 dh_0 \\
\bar{u}_y(\mathbf{x}_p, w) &= \int_S [\bar{u}_x(\mathbf{x}_0, w)] \left\{ \frac{1}{4p^2} \int_{-\infty}^{\infty} \int_{-\infty}^{\infty} \left[\frac{2ik_y \mathbf{n}'}{F} \right] A^* e^{-n z_0 - ik_x(x-x_0) - ik_y(y-y_0)} dk_x dk_y \right. \\
&\quad + \frac{1}{4p^2} \int_{-\infty}^{\infty} \int_{-\infty}^{\infty} \left[\frac{ik_y(2k^2 - k_s^{*2})}{Fk^2} \right] B^* e^{-n z_0 - ik_x(x-x_0) - ik_y(y-y_0)} dk_x dk_y \\
&\quad \left. + \frac{1}{4p^2} \int_{-\infty}^{\infty} \int_{-\infty}^{\infty} \left[\frac{ik_x}{k^2 \mathbf{n}'} \right] C^* e^{-n z_0 - ik_x(x-x_0) - ik_y(y-y_0)} dk_x dk_y \right\} d\mathbf{x}_0 dh_0 \\
\bar{u}_z(\mathbf{x}_p, w) &= \int_S [\bar{u}_x(\mathbf{x}_0, w)] \left\{ \frac{1}{4p^2} \int_{-\infty}^{\infty} \int_{-\infty}^{\infty} \left[-\frac{(2k^2 - k_s^{*2})}{F} \right] A^* e^{-n z_0 - ik_x(x-x_0) - ik_y(y-y_0)} dk_x dk_y \right. \\
&\quad \left. + \frac{1}{4p^2} \int_{-\infty}^{\infty} \int_{-\infty}^{\infty} \left[-\frac{2n}{F} \right] B^* e^{-n z_0 - ik_x(x-x_0) - ik_y(y-y_0)} dk_x dk_y \right\} d\mathbf{x}_0 dh_0
\end{aligned} \tag{20}$$

where parameters A^* , B^* and C^* are defined by

$$\begin{aligned}
A^* &= -\sin a \left[\sin 2d \cdot (k_x^2 + n^2) + \cos 2d \cdot 2ik_x n \right] \\
&\quad - \cos a \left[\sin d \cdot 2k_x k_y + \cos d \cdot 2ik_y n \right] \\
B^* &= \sin a \left[\sin 2d \cdot (k_x^2 + k^2) \mathbf{n}' + \cos 2d \cdot ik_x (2k^2 - k_s^{*2}) \right] \\
&\quad + \cos a \left[\sin d \cdot 2k_x k_y \mathbf{n}' + \cos d \cdot ik_y (2k^2 - k_s^{*2}) \right] \\
C^* &= \sin a \left[\sin 2d \cdot (-k_x k_y) + \cos 2d \cdot (-ik_y \mathbf{n}') \right] \\
&\quad + \cos a \left[\sin d \cdot (k_x^2 - k_y^2) + \cos d \cdot ik_x \mathbf{n}' \right]
\end{aligned} \tag{21}$$

Finally, based on the Fourier transformation between frequency domain and time domain, the time histories of near-fault ground motions can be determined.

NUMERICAL EXAMPLE FOR A THRUST FAULT

Consider a reserve slip fault plane ($a=\pi/2$) buried in a half-space with longitudinal and shear wave velocities of $C_p=5.6$ km/sec and $C_s=3.2$ km/sec, respectively. The hypocenter and the dip angle are defined as $\mathbf{x}_A=(0,0,13)$ km and $d=40^\circ$. The dislocation $[\bar{u}_x(\mathbf{x}_0; w)]$ can be determined from the Fourier

transformation of the slip function $D(x_0;t)$ that is defined by Eq. (5) under the specified condition of $x_R=6.0\text{km}$, $x_0=5.25\text{km}$, $v=2.4\text{ km/s}$, and $D_0=0.5\text{ sec}$. Furthermore, the maximum dislocation is scaled to become 1.5 m.

Based on the proposed methodologies, the induced near-fault ground motions can be determined. The simulated time histories of ground displacement and velocity for observation points along x -, y -axes and P-P' line (with an angle of $\pi/4$ from x -axis) are compared in Fig. 4. The representative pulse-like velocity waveforms can be found within the near-fault area where the rupture front and healing front are close to each other to cause interference, and the duration of the pulse is about 1.0 second. The contours of the induced PGV are shown in Fig. 5, where the circles denoting the ground observation points specified in this earthquake scenario.

Based on the simulated time histories of ground acceleration, the associated near-fault response spectra can be determined. Figure 6 illustrates the response spectrum shapes (spectral acceleration, velocity and displacement) for observation points located along x -, y -axes and P-P' line, and the contour maps of the spectral acceleration demands at structural period of 1.0 second are shown in Figure 7. It can be found from Figs. 5 and 7 that the variation of near-fault spectral demands is coincident with that of the representative ground velocity pulse.

CONCLUSIONS

In this paper, a quasi-dynamic rupture model of a buried dip-slip fault is defined. Then, based on the integral representation theory, the ground motions of a three dimensional half-space can be determined by means of the slip function of a buried fault plane as well as the Green's function due to a unit point source within the half-space. In consequence of the directivity effect, the representative pulse-like velocity waveforms can be found within the near-fault area owing to the interference of the rupture and healing fronts. Therefore, instead of the scarcely observed near-fault ground motions, the near-fault structural response spectra can be studied by the simulated representative pulse-like ones to show the attenuation of required spectral demands for designing structures against the near-fault ground motions. It can be found from the earthquake scenario caused by a reverse slip fault that the distribution of spectral demands is coincident with that of the representative ground velocity pulse, and in general, the near-fault impact in x -direction (perpendicular to the fault) is larger than that in y -direction (parallel to the fault).

REFERENCES

- Alavi, B. and Krawinkler, H., (2000). Consideration of near-fault ground motion effects in seismic design. *12th WCEE Proc.*, Auckland, New Zealand.
- Boatwright, J. (1981). Quasi-dynamic models of simple earthquakes: application to an aftershock of the 1975 Oroville, California, Earthquake, *Bull. Seism. Soc. Am.* **71**, 69-94.
- Madariaga, R. (1976). Dynamics of an expanding circular fault. *Bull. Seism. Soc. Am.* **66**, 639-666.
- Somerville, P.G., Smith, N.F., Graves, R.W. and Abrahamson, N.A. (1997). Modification of empirical strong ground motion attenuation relations to include the amplitude and duration effects of rupture directivity. *Seismological Research Letters* **68**, 199-222.
- Pao, Y. H. and V. Varatharajulu (1976), Huygens' principle, radiation conditions, and integral formulas for the scattering of elastic waves, *J. Acoust. Soc. Am.*, **59**, 1361-1371.

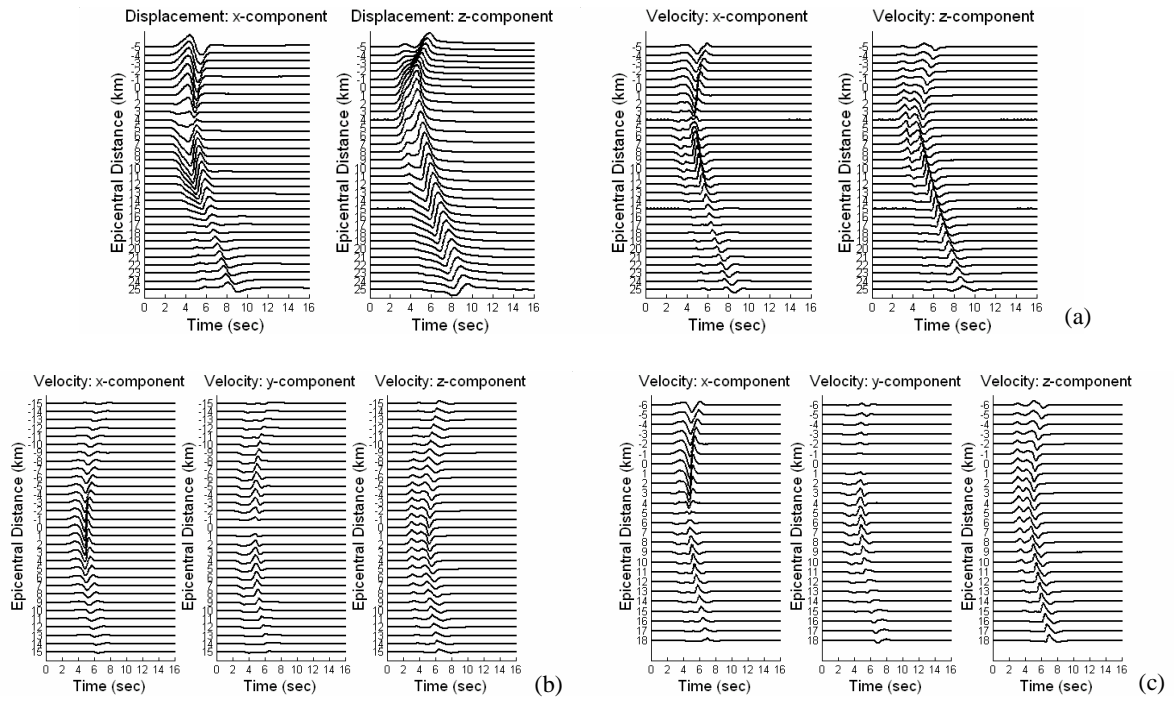


Fig. 4: Time histories of (a) ground displacement and velocity along x -axis (zero for y -component), (b) ground velocity along y -axis and (c) along P-P' line ($\pi/4$ from x -axis)

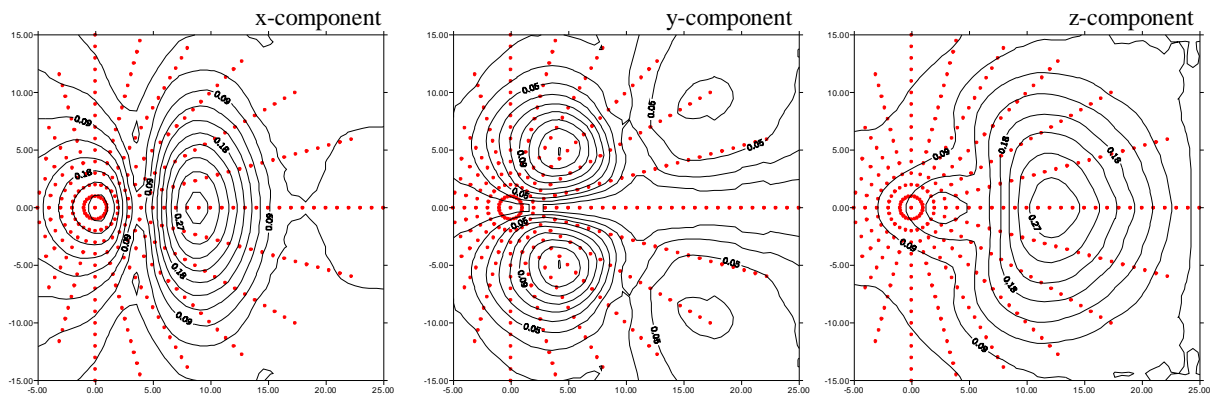


Fig. 5: Distribution of contour maps for the induced PGV

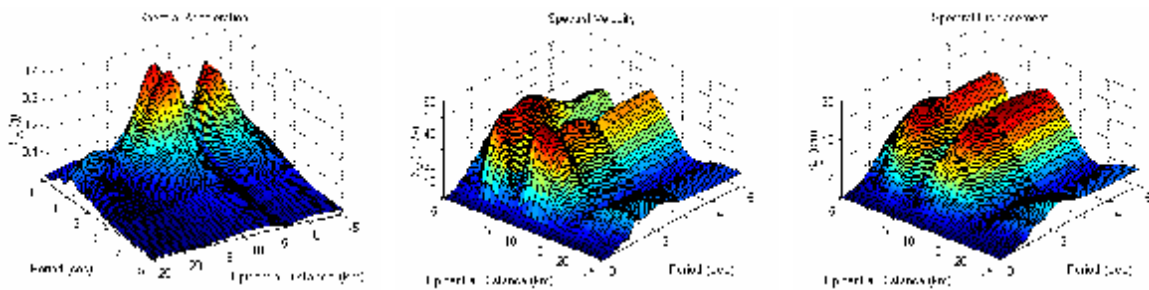


Fig. 6(a): Horizontal response spectrum shapes (x-component) for observation points along x -axis

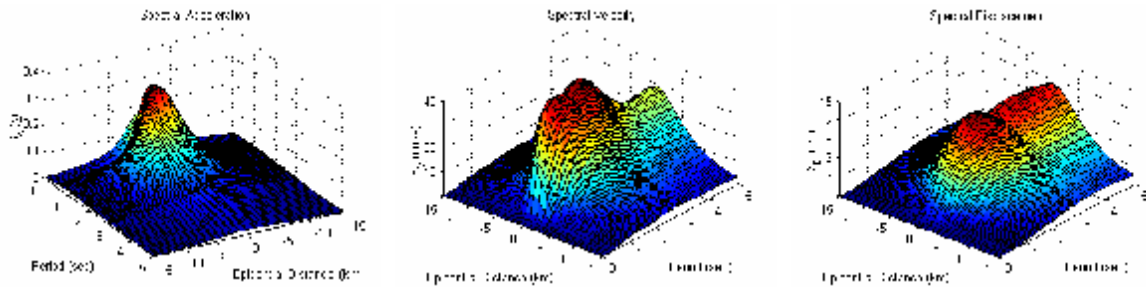


Fig. 6(b): Horizontal response spectrum shapes (x-component) for observation points along y-axis

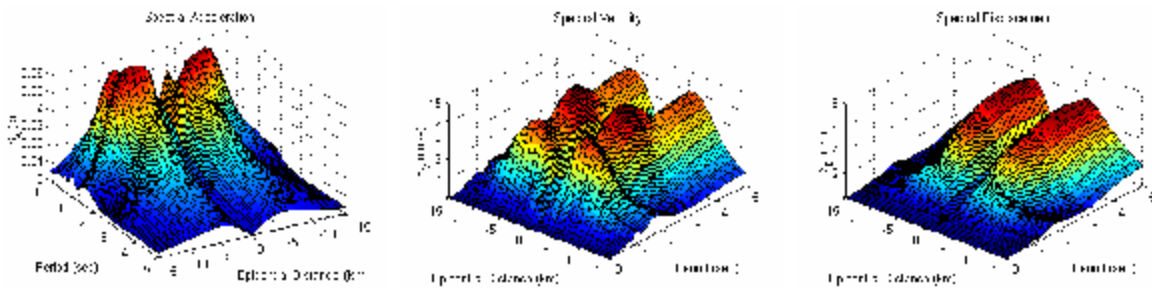


Fig. 6(c): Horizontal response spectrum shapes (y-component) for observation points along y-axis

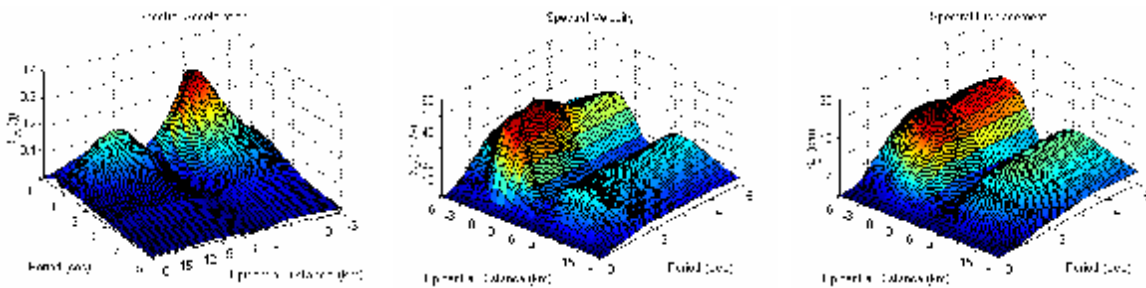


Fig. 6(d): Horizontal response spectrum shapes (x-component) for observation points along P-P' line

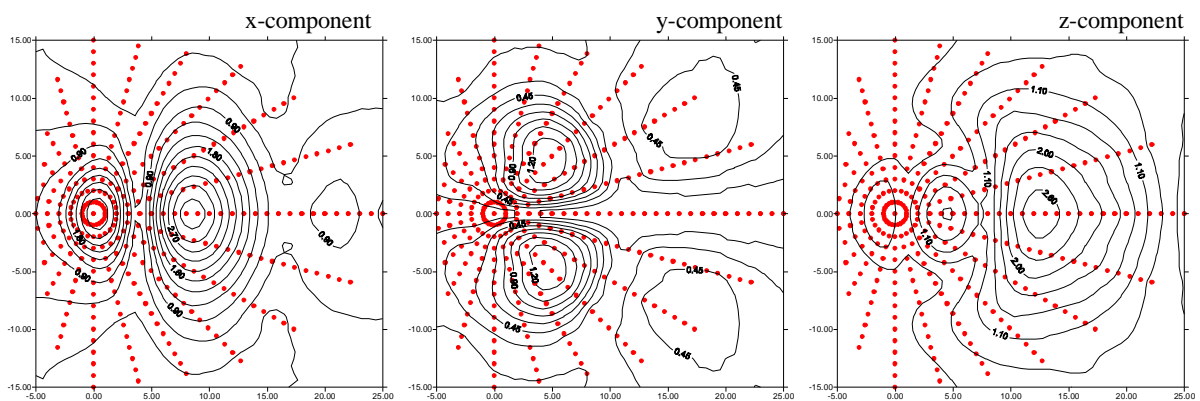


Fig. 7: Contour maps of spectral acceleration demands (unit: m/s^2) at structural period of 1.0 second